

Comparison of Structure-Preserving Methods for the Cahn-Hilliard-Navier-Stokes Equations

Jimmy Kornelije Gunnarsson^[0009-0000-7610-6360] and
Robert Klöfkor^[0000-0001-9664-0333]

Abstract We develop structure-preserving discontinuous Galerkin methods for the Cahn-Hilliard-Navier-Stokes equations with degenerate mobility. The proposed SWIPD-L and SIPGD-L methods incorporate parametrized mobility fluxes with edge-wise mobility treatments for enhanced coercivity-stability control. We prove coercivity for the generalized trilinear form and demonstrate optimal convergence rates while preserving mass conservation, energy dissipation, and the discrete maximum principle. Comparisons with existing SIPG-L and SWIP-L methods confirm similar stability. Validation on hp -adaptive meshes for both standalone Cahn-Hilliard and coupled systems shows significant computational savings without accuracy loss.

1 Introduction

Consider the spatial domain $\Omega \subset \mathbb{R}^d$, $d = 2, 3$, with Lipschitz continuous boundary $\partial\Omega$ and the time interval $(0, T]$ for $T \in \mathbb{R}^+$. The Cahn-Hilliard (CH) equations model phase separation in binary mixtures for a phase-field $\psi : \Omega \times (0, T] \rightarrow [-1, 1]$ following:

$$\partial_t \psi + \nabla \cdot (\psi \mathbf{u}) - \nabla \cdot Pe^{-1}(M(\psi)\nabla v) = 0, \quad (1)$$

$$v + Cn^2 \Delta \psi - W'(\psi) = 0, \quad (2)$$

where $Pe > 0$ is the Peclet number, \mathbf{u} is an advection field, v is the chemical potential, $W(\psi) := \frac{1}{4}(1 - \psi^2)^2$ is the double-well potential, and $M(\psi) := \max\{1 - \psi^2, 0\}$ is the

Jimmy Kornelije Gunnarsson
Centre for Mathematical Sciences, Lund University, Box 117, 22100 Lund, Sweden e-mail: jimmy_kornelije.gunnarsson@math.lu.se

Robert Klöfkor
Centre for Mathematical Sciences, Lund University, Box 117, 22100 Lund, Sweden e-mail: robertk@math.lu.se

mobility function. We equip Eq.(1) with homogeneous Neumann boundary conditions $\mathbf{n} \cdot \nabla \psi = 0$ and $\mathbf{n} \cdot \nabla v = 0$ on $\partial\Omega$.

We present below a special case of a fundamental theorem for boundedness.

Theorem 1 (Boundedness [5]) *Suppose that Ω is convex and that the initial phase-field satisfies $\psi^0 \in H^1(\Omega)$ and $\|\psi^0\|_{L^\infty(\Omega)} \leq 1$. Then, if the mobility function $M(\psi)$ is defined as above, and $\int_\Omega M(\psi^0) + W(\psi^0) < C$ for $C > 0$, then the weak solution $\psi \in H^1(\Omega)$ of the CH equation satisfies a weak maximum principle, i.e., $\|\psi\|_{L^\infty(\Omega)} \leq 1$ for $t \in (0, T]$.*

While Theorem 1, proven in [5, Thm. 1], guarantees a weak maximum principle at the continuum level for a degenerate mobility, achieving discrete boundedness remains a significant challenge. The standard Finite Element Method (FEM), symmetric weighted interior penalty (SWIP), and symmetric interior penalty Galerkin (SIPG) discretizations fail to preserve boundedness without additional stabilization [8], even when using the degenerate mobility M . Recent work, however, has demonstrated that boundedness can be numerically achieved through carefully designed limited Galerkin schemes, including FEM-L for FEM, and for DG SIPG-L, and SWIP-L [8] with degenerate CH.

In this work, we extend these structure-preserving methods by introducing new mobility fluxes using the Discontinuous Galerkin (DG) formulations with intersection-wise mobility treatments. These extend the SWIP-L and SIPG-L methods introduced in [8], by allowing for better control of the coercivity-stability balance.

Boundedness of the CH equations is in particular important when coupled to the incompressible Navier-Stokes (NS) equations:

$$\rho(\psi)(\partial_t \mathbf{u} + \mathbf{u} \cdot \nabla \mathbf{u}) + \mathbf{J} \cdot \nabla \mathbf{u} + \nabla \cdot (P\mathbb{I} - \mu(\psi)D(\mathbf{u})) = \frac{1}{WeCn} \nu \nabla \psi \quad (3)$$

$$\nabla \cdot \mathbf{u} = 0 \quad (4)$$

where $\rho(\psi) := \frac{1+\psi}{2}\rho_1 + \frac{1-\psi}{2}\rho_2$ is the density, $\mathbf{J} := \frac{\rho_2 - \rho_1}{2} P e^{-1} M(\psi) \nabla v$ is the mass flux, P is the pressure, $\mu(\psi) := \frac{1+\psi}{2}\mu_1 + \frac{1-\psi}{2}\mu_2$ is the viscosity, and $D(\mathbf{u}) = \frac{1}{2}(\nabla \mathbf{u} + \nabla \mathbf{u}^T)$ is the rate of deformation tensor, where \mathbb{I} denotes the identity tensor. Moreover, ρ_j and μ_j are the characteristic densities and viscosities for phases $j = 1, 2$, respectively. We equip the boundary conditions $\mathbf{n} \cdot \mathbf{u}|_{\partial\Omega} = \mathbf{n} \cdot \nabla P|_{\partial\Omega} = 0$. We note that the expected bounds for the physical mass density $\rho \in [\rho_1, \rho_2]$ follows directly from boundedness of the phase-field $\psi \in [-1, 1]$.

The main contributions of this paper are: (i) the development of SWIPD-L and SIPGD-L methods with a parametrized mobility flux for enhanced stability, (ii) a proof of coercivity for the generalized trilinear form for SWIPD and SIPGD schemes, and (iii) numerical validation demonstrating optimal convergence rates and structure preservation for both standalone CH and coupled CHNS systems. We compare the performance of SIPG-L, SWIP-L, SIPGD-L, and SWIPD-L methods through extensive numerical experiments, including hp -adaptive formulations for our new schemes.

2 Discretization

In this section, we consider the spatial and temporal discretization of the CHNS equation system. Our main focus is to motivate the design of the SWIPD-L and SIPGD-L methods and to provide a proof of coercivity for the resulting trilinear form, while the remaining details follow a similar procedure as in [8].

Let the spatial domain Ω be partitioned into a union of M non-intersecting elements K forming a mesh $\mathcal{T}_h = \cup_{i=1}^M K_i$. Then we denote by Γ_i with unit normal \mathbf{n} the set of all intersections between two elements of the grid \mathcal{T}_h , and the set of all intersections, also with the boundary of the domain Ω , is denoted by Γ . For an intersection $e \in \Gamma$ we denote the adjacent elements with K_e^- and K_e^+ ($K_e^- = K_e^+$ for $e \in \Gamma \cap \Gamma_i$) and define

$$h_e := \frac{2|K_e^-||K_e^+|}{|e|(|K_e^-| + |K_e^+|)} \quad \forall e \in \Gamma. \quad (5)$$

The global mesh width is then defined as $h = \max_{e \in \Gamma} h_e$. For the time discretization we consider a uniform partition of the time interval $[0, T]$ with time increment $\tau = \frac{T}{N}$ for some $N \in \mathbb{N}$ and denote the time levels with $t_n = n \cdot \tau$ for $n = 0, 1, \dots, N$. For brevity we will also denote time-dependent variables with a subscript n , i.e., $\psi^n = \psi(\cdot, t_n)$.

Following standard FEM notation we consider a general order FEM formulation for the function space of trial and test functions:

$$V_h^p = \{\varphi \in L^2(\mathcal{T}_h) : \varphi|_K \in \mathbb{P}^p(K), \forall K \in \mathcal{T}_h\}, \quad (6)$$

where $\mathbb{P}^p(\mathcal{T}_h)$ denotes a polynomial space of order at most p on the grid \mathcal{T}_h . We also permit p -adaptivity over the mesh \mathcal{T}_h , and as such, the polynomial order p may vary across elements K , and we denote the local polynomial order as p_K . We denote the maximal permitted polynomial order as p_{\max} , and the minimal order as p_{\min} . We describe the application further in Sec. 2.2.

Before proceeding, we introduce operators $[\cdot]$, $\{\cdot\}$ and $\langle \cdot \rangle$ for $e \in \Gamma_i$ as

$$[\varphi] = \varphi|_{K_e^-} - \varphi|_{K_e^+}, \quad \{\varphi\} = \frac{1}{2} (\varphi|_{K_e^-} + \varphi|_{K_e^+}), \quad \langle \varphi \rangle = \frac{2 \varphi|_{K_e^+} \varphi|_{K_e^-}}{\varphi|_{K_e^+} + \varphi|_{K_e^-}},$$

for some φ , where $\{\cdot\}$ and $\langle \cdot \rangle$ denote the arithmetic and harmonic averages, respectively. To simplify the notation $\varphi^\pm := \varphi|_{K_e^\pm}$ is also used frequently. Moreover, we introduce the subscript $\varphi_\oplus := \max\{0, \varphi\}$ and $\varphi_\ominus := \min\{0, \varphi\}$ to denote the positive and negative restriction of a function, respectively. This notation will in particular be utilized for upwinding.

2.1 Discontinuous Galerkin

Given a degenerate mobility function $M : V_h^p \rightarrow [0, 1]$, we introduce the trilinear form $b : L^\infty(\mathcal{T}_h) \times V_h^p \times V_h^p \rightarrow \mathbb{R}$:

$$b(M(\psi_h), v_h, \varphi) = \int_{\mathcal{T}_h} M(\psi_h) \nabla v_h \cdot \nabla \varphi \, dx + \sum_{e \in \Gamma} \int_e \frac{\eta_e \Lambda_e(M(\psi_h))}{h_e} [v_h] [\varphi] - F(M(\psi_h), v_h) [\varphi] - F(M(\psi_h), \varphi) [v_h] ds, \quad (7)$$

where $\eta_e \geq 0$ is a penalty parameter over e , F is the mobility flux, and $\Lambda_e(M(\psi_h))$ is a mobility flux function. We examine the coercivity properties arising from the degeneracy of M . We consider the following formulations for F :

$$F(M(\psi_h), v_h) = \langle M(\psi_h) \rangle \{ \nabla v_h \}, \quad F(M(\psi_h), v_h) = \{ M(\psi_h) \nabla v_h \}, \quad (8)$$

corresponding to a weighted average with a harmonic average for the mobility flux $\langle M(\psi_h) \rangle$ and an arithmetic average $\{ M(\psi_h) \nabla v_h \}$, which correspond to the SWIP and SIPG discretization, respectively. We note that the SWIP formulation with $\langle M(\psi_h) \rangle$ follows from choosing the weights $w^\pm = \frac{M(\psi_h)^\mp}{M(\psi_h)^+ + M(\psi_h)^-}$, as suggested in [7] for treating a diffusion-type formulation for DG.

Lemma 1 (Trace inequality, [9]) *Consider an intersection $e \in \Gamma_i$ shared by two elements K_e^- and K_e^+ . Then for $K \in \mathcal{T}_h$ there exists a constant $C_K > 0$ independent of the mesh width h such that for all $\varphi_h \in V_h^p$ for $p > 0$ and $e \in \Gamma_i$ the following inequality holds:*

$$\| \nabla \varphi_h^\pm \cdot \mathbf{n}^+ \|_{L^2(e)}^2 \leq \frac{|e|}{|K_e^\pm|} C_{K_e^\pm} \| \nabla \varphi_h \|_{L^2(K_e^\pm)}^2, \quad (9)$$

where, in the special case of K_e being a quadrilateral or triangle, $C_{K_e^\pm} = \frac{p_K(p_K+d-1)}{d}$ where p_K is the local polynomial degree (see further treatments and formulations in [1] and [6]).

Lemma 2 (Trace inequality for mixed polynomial order) *Under the same setting as in Lemma 1 and for $\varphi_h \in V_h^p$ the following inequality holds for all $e \in \Gamma_i$:*

$$\| \{ \nabla \varphi \cdot \mathbf{n} \} \|_{L^2(e)}^2 \leq \frac{C_e}{2h_e} \left(\| \nabla \varphi^+ \cdot \mathbf{n}^+ \|_{L^2(K_e^+)}^2 + \| \nabla \varphi^- \cdot \mathbf{n}^+ \|_{L^2(K_e^-)}^2 \right), \quad (10)$$

where for the special case when K_e is a quadrilateral or triangle:

$$C_e = \max_{p \in \{p_{K_e^+}, p_{K_e^-}\}} \frac{p(p+d-1)}{d}. \quad (11)$$

Proof. The proof follows from the triangle inequality and the trace inequality in Lemma 1:

$$\| \{ \nabla \varphi \cdot \mathbf{n} \} \|_{L^2(e)}^2 \leq \frac{1}{2} \left(\| \nabla \varphi^+ \cdot \mathbf{n} \|_{L^2(e)}^2 + \| \nabla \varphi^- \cdot \mathbf{n} \|_{L^2(e)}^2 \right), \quad (12)$$

then upon applying the trace inequality in Lemma 1 we obtain the desired result by then maximizing the quantity

$$\frac{|e|}{|K_e^+|} C_{K_e^+} + \frac{|e|}{|K_e^-|} C_{K_e^-} \leq \frac{C_e}{h_e}, \quad (13)$$

for a joint inequality. \square

Theorem 2 (Coercivity) Consider a fixed phase-field $\psi_h \in V_h^p$ for $p > 0$ satisfying $M(\|\psi_h\|_{L^\infty(\overline{\mathcal{T}}_h)}) \geq \delta$ for some small $\delta > 0$. Then for $v_h \in V_h^p$ there exists a constant $\eta_e > 0$ and mobility flux Λ_e independent of the mesh width h such that for $e \in \Gamma_i$ the trilinear form b in Eq.(7) is coercive such that for the DG semi-norm

$$\|v_h\|_{DG}^2 = \|\sqrt{M(\psi_h)}\nabla v_h\|^2 + \sum_{e \in \Gamma_i} \int_e \frac{\Lambda_e(M(\psi_h))\eta_e}{h_e} [v_h]^2 ds,$$

for some $C > 0$ where $\|v_h\|_{DG}^2 \leq C b(M(\psi_h), v_h, v_h)$. Then the following coercivity condition holds:

$$\eta_e \geq \max_{p \in \{K_e^+, K_e^-\}} p(p+d-1), \quad \Lambda_e(M(\psi_h)) \geq \tilde{M}_e^{2\alpha}(\psi_h)\lambda^*, \quad (14)$$

where for $\alpha \in [0, \frac{1}{2}]$ the maximum contrast λ^* is defined as

$$\lambda^* = \max_{K \in \mathcal{T}_h} \sum_{e \in \partial K} \frac{\|\tilde{M}_e(\psi_h)\|_{L^\infty(e)}^{2-2\alpha}}{\min_{x \in K} M(\psi_h(x))}, \quad (15)$$

and the flux $\tilde{M}_e(\psi_h)$ is defined as

$$\tilde{M}_e(\psi_h) = \langle M(\psi_h) \rangle, \quad \tilde{M}(\psi_h) = \max\{M(\psi_h^+), M(\psi_h^-)\}, \quad (16)$$

for the SWIP and SIPG mobility fluxes, respectively.

Proof. The overall proof follows similarly to the one in [8, Theorem 3.2], with the main difference being the treatment of the mobility term $M(\psi_h)$ for the first Cauchy-Schwarz inequality over the intersections $e \in \Gamma_i$. In particular we note that for $e \in \Gamma_i$ we have

$$|F(M(\psi_h), v_h)[v_h]| \leq \|\tilde{M}(\psi_h)^{1-\alpha}\{\nabla v \cdot \mathbf{n}_{K_e^+}\}\|_{L^2(e)} \|\tilde{M}(\psi_h)^\alpha [v_h]\|_{L^2(e)}, \quad (17)$$

Following a similar approach to the proof in [8], which considered $\alpha = 0$, we generalize to a free variable $\alpha \in [0, \frac{1}{2}]$ to obtain the desired result by also applying the modified trace inequality in Lemma 2 and maximizing the resulting quantity for a joint inequality over the intersection e . \square

For the remainder of this study we will consider the regularization $M_\delta(\psi_h) = \max\{M(\psi_h), \delta\}$ for some small $\delta > 0$ to ensure the coercivity condition in Theorem 2 is satisfied, and we will simply denote this regularized mobility as $M(\psi_h)$ for brevity and we pick $\delta = 10^{-20}$ (practically 0) for the numerical simulations.

Remark 1 (mobility flux) It is complicated to estimate the maximum contrast λ^* for a sharp estimate. For simplicity, it is sufficient to consider the mobility flux as $\Lambda_e = \beta \tilde{M}_e^{2\alpha}(\psi_h)$ for some constant a-priori estimate $\beta \geq \lambda^*$. For instance, $\beta = 5$ was considered in the numerical experiments in [8].

Corollary 1 (Case V_h^0) For the case of V_h^0 the coercivity condition in Thm. 2 reduces to

$$\eta_e \geq 1, \quad \Lambda_e(M(\psi_h)) \geq \tilde{M}(\psi_h). \quad (18)$$

Proof. Since for $\varphi \in V_h^0$ then $\nabla\varphi = 0$ and thus only the penalty term remains in the trilinear form b in Eq.(7), and consequently the coercivity condition reduces to $\eta_e \Lambda_e(M(\psi_h)) \geq \tilde{M}(\psi_h)$, which is satisfied for the stated conditions. \square

Similarly to Eq.(7) we introduce the following bilinear form for the discretization of the Laplacian operator in Eq.(1):

$$a(\psi_h, \varphi) = \int_{\mathcal{T}_h} \nabla\psi_h \cdot \nabla\varphi \, dx + \sum_{e \in \Gamma} \int_e \frac{\eta_e^\Delta}{h_e} [\psi_h] [\varphi] - \{\nabla\psi_h \cdot \mathbf{n}\} [\varphi] - \{\nabla\varphi \cdot \mathbf{n}\} [\psi_h] ds, \quad (19)$$

where $\eta_e^\Delta \geq \eta_e$ is a local penalty parameter for the Laplacian operator. We introduce the superscript Δ to distinguish the penalty parameter for the Laplacian from the one for the mobility term in Eq.(7), and in particular, to lump the constants in practice so that $\eta_e^\Delta = \beta\eta_e$ for some $\beta \geq 1$ following Rmk. 1.

When we consider advection coupling we introduce the standard upwinding for the advection term:

$$c(\mathbf{u}, \psi_h, \varphi) = \int_{\mathcal{T}_h} \mathbf{u} \cdot \nabla\varphi \psi_h \, dx - \sum_{e \in \Gamma_i} \int_e (\{\mathbf{u} \cdot \mathbf{n}^+\}_{\oplus} \psi_h^+ + \{\mathbf{u} \cdot \mathbf{n}^+\}_{\ominus} \psi_h^-) [\varphi] ds, \quad (20)$$

Thus, we have introduced all the DG-specific bilinear and trilinear forms for the spatial discretization of the CH equations. In the following, we consider the time discretization and coupling to the NS equations.

To treat the non-linear term W we introduce the Eyre splitting:

$$\Phi^+(\psi_h) = \psi_h^3, \quad \Phi^-(\psi_h) = -\psi_h, \quad (21)$$

where clearly $W(\psi_h) = \Phi^+(\psi_h) + \Phi^-(\psi_h)$. Below we present our proposed schemes for the CH equations:

$$\frac{1}{\tau} \langle \psi_h^n - \psi_h^{n-1}, \varphi \rangle - c(\tilde{\mathbf{u}}^{n-\frac{1}{2}}, \psi_h^n, \varphi) + Pe^{-1} b(M(\psi_h^n), v_h^n, \varphi) = 0, \quad (22)$$

$$\langle v_h^n, \xi \rangle - \langle \Phi^+(\psi_h^n) + \Phi^-(\psi_h^{n-1}), \xi \rangle - Cn^2 a(\psi_h^n, \xi) = 0, \quad (23)$$

for $\xi, \varphi \in V_h^p$ and $\tilde{\mathbf{u}}^{n-\frac{1}{2}}$ being the velocity field at time step $n - \frac{1}{2}$. We note that the mobility term, and penalty weights, are treated implicitly in time. The main difference between the proposed schemes is the mobility flux for the penalty term, where we consider both a harmonic average and an intersection maximum as described in Eq.(7). The outline and algorithm of the scheme are very similar to those detailed in [8], as it is simply an algebraic reformulation of the same scheme with a different mobility flux for the penalty term, therefore we do not repeat the details here.

For the Navier-Stokes coupling we follow exactly the same formulation as in [8] with a post-processing step. Our modification includes projecting the FEM velocity field \mathbf{u} to a Brezzi-Douglas-Marini space of first order to obtain a divergence-free velocity field $\tilde{\mathbf{u}}$.

Definition 1 (Phase-field mass) We refer to the quantity

$$m_{\psi_h} = \frac{1}{|\mathcal{T}_h|} \int_{\mathcal{T}_h} \psi_h dx \quad (24)$$

with $|\mathcal{T}_h| = \int_{\mathcal{T}_h} 1 dx$ as the phase-field mass.

Definition 2 (Discrete energy) We refer to the quantity:

$$\mathcal{E}[\psi_h, \mathbf{u}] = \frac{1}{WeCn} \int_{\mathcal{T}_h} W(\psi_h) + \frac{Cn^2}{2} a(\psi_h, \psi_h) dx + \int_{\mathcal{T}_h} \rho(\psi_h) \frac{|\mathbf{u}|^2}{2} dx, \quad (25)$$

as the discrete energy.

Following similar arguments as in [8] and references therein, the provided schemes are energy dissipative and mass conservative on the discrete level for the quantities defined in Definitions 1 and 2.

2.2 Limiter and hp -adaptivity

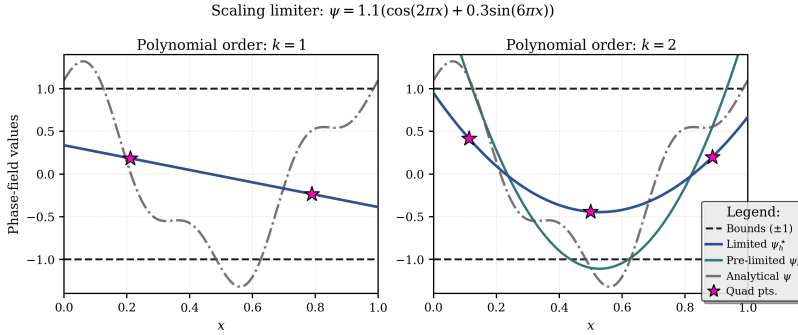


Fig. 1 Example of a scaling limiter for local \mathbb{P}^2 phase-field ψ_h

A Zhang-Shu scaling limiter [10] is applied to ψ_h , with quadrature evaluation for local polynomial order $p_K \geq 1$. The limiter structure is outlined in Fig. 2.2 and described in [8]. Following the notation in [8] we denote by SWIPD-L and SIPGD-L the methods corresponding to the mobility flux with $\alpha = \frac{1}{2}$ in Theorem 2, while the methods with $\alpha = 0$ are denoted by SWIP-L and SIPG-L, respectively. We note that the mobility flux with $\alpha = \frac{1}{2}$ corresponds to a more diffusive flux, which facilitates treatment over the intersections e , at the potential cost of a larger global contrast λ^* .

For h -adaptivity we follow the formulation provided in [8] and we consider an indicator function $H(\psi_h) := \frac{(1-\psi^2)}{4}$ and refinement for elements K where $H(\psi_h) < 0.0525$, and coarsening is suggested when $H(\psi_h) > 0.15$. Meanwhile, for p -adaptivity, coarsening is performed for elements K where $H(\psi_h) > 0.075$ and refinement follows similarly

to h -adaptivity. Fig. 2 shows an example of hp -adaptivity. We note that the thresholds for refinement and coarsening are somewhat arbitrary and can be tuned for better performance.

In particular, we aim to isolate elements K with low-order polynomials that satisfy $\|\psi_h\|_{L^\infty(K)} \approx 1$ to ensure that coercivity is not broken by populating elements with low-order polynomials with values close to the bounds, which can ideally lead to a smaller contrast λ^* and less penalization in the scheme. Such effects are examined in Section 3, where we compare the performance of h -adaptivity and hp -adaptivity for the proposed schemes. Moreover, to allow $p_{\min} = 0$ we consider $\eta_e =$

$$\max_{p \in \{p_{K_e^+}, p_{K_e^-}\}} \max \{p(p + d - 1), 1\}.$$

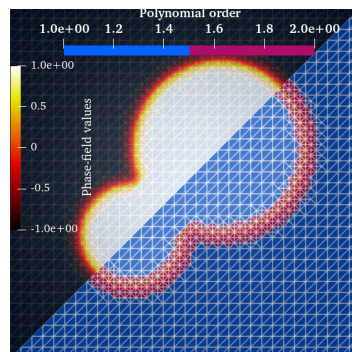


Fig. 2 Ex. 3 with hp -adaptivity for $p_{\min} = 1$ and $p_{\max} = 2$ at time $t = 0$.

3 Numerics

In this section, we present numerical results for the proposed schemes for both the standalone CH equations and the coupled CH-NS system. We first consider Ex. 1 to verify the optimal convergence rates in 2D and 3D. We then investigate the performance of the proposed schemes for merging droplets in Ex. 2, and finally consider the rotating droplet configuration in Ex. 3 for the coupled CH-NS system to demonstrate the structure-preserving properties and hp -adaptivity. The numerical simulations are implemented in DUNE-FEM [2, 3] at version 2.11 with its Python interface [4].

Example 1 (Artificial trigonometric solution) Consider the domain $\Omega = [0, 1]^d$ and the following artificial solution to the CH equations $\psi(\mathbf{x}, 0) = A \prod_{i=1}^d \cos(4\pi x_i)$ where $A \in (0, 1]$ is an amplitude parameter and x_i is the i -th component of the spatial coordinate \mathbf{x} . We then consider the following forcing term $S(\mathbf{x}, t) = Pe^{-1} \nabla \cdot (M(\psi)(Cn^2 \Delta \psi - W'(\psi)))$ added to the right-hand side of Eq.(22), where $Cn = 0.1$, $Pe = 0.3$ are the Cahn and Peclet numbers respectively. The simulation is run for $t \leq T = 0.01$.

In Table 1, we present the L^2 and H^1 errors and EOC for Ex. 1 for the different schemes with amplitudes $A = 0.1$ and $A = 0.6$ and $\beta = 5$. The results are consistent with the theoretically expected convergence rates. Additionally, SWIPD-L/SIPGD-L and SWIP-L/SIPG-L yield identical errors and EOC, which is consistent with the fact that the mobility flux does not affect the consistency of the scheme, but only the stability and coercivity. Similar behavior for SIPG-L and SWIP-L was also observed in [8]. We also tested if the same convergence rates hold in 3D, and the results are presented in Table 2 for $A = 0.1$ and $\tau = 10^{-3} \cdot 2^{-\frac{N}{16}}$. The observed rates confirm the theoretical predictions.

Table 1 Ex. 1: L^2 and H^1 errors and EOC for $A = 0.1$ and $A = 0.6$ and $\tau = 10^{-(2+p)} \cdot 2^{-\frac{N-32}{32}}$ for $p \in \{1, 2\}$ and N being the number of elements in each axis.

Scheme, p	N	$A = 0.1$				$A = 0.6$			
		L^2 Error		H^1 Error		L^2 Error		H^1 Error	
		Error	EOC	Error	EOC	Error	EOC	Error	EOC
SIPG-L, 1	32	1.29e-03	—	1.01e-01	—	7.14e-03	—	6.05e-01	—
	64	3.41e-04	1.92	5.04e-02	1.00	1.88e-03	1.92	3.02e-01	1.00
	128	8.75e-05	1.96	2.52e-02	1.00	4.82e-04	1.97	1.51e-01	1.00
	256	2.21e-05	1.98	1.26e-02	1.00	1.22e-04	1.98	7.56e-02	1.00
SIPG-L, 2	32	2.19e-05	—	5.10e-03	—	1.32e-04	—	3.06e-02	—
	64	2.72e-06	3.01	1.28e-03	2.00	1.63e-05	3.01	7.66e-03	2.00
	128	3.40e-07	3.00	3.19e-04	2.00	2.04e-06	3.00	1.91e-03	2.00
	256	4.25e-08	3.00	7.98e-05	2.00	2.55e-07	3.00	4.79e-04	2.00
SWIP-L, 1	32	1.29e-03	—	1.01e-01	—	7.14e-03	—	6.05e-01	—
	64	3.41e-04	1.92	5.04e-02	1.00	1.88e-03	1.92	3.02e-01	1.00
	128	8.75e-05	1.96	2.52e-02	1.00	4.82e-04	1.97	1.51e-01	1.00
	256	2.21e-05	1.98	1.26e-02	1.00	1.22e-04	1.98	7.56e-02	1.00
SWIP-L, 2	32	2.19e-05	—	5.10e-03	—	1.32e-04	—	3.06e-02	—
	64	2.72e-06	3.01	1.28e-03	2.00	1.63e-05	3.01	7.66e-03	2.00
	128	3.40e-07	3.00	3.19e-04	2.00	2.04e-06	3.00	1.91e-03	2.00
	256	4.25e-08	3.00	7.98e-05	2.00	2.55e-07	3.00	4.79e-04	2.00
SIPGD-L, 1	32	1.29e-03	—	1.01e-01	—	7.14e-03	—	6.05e-01	—
	64	3.41e-04	1.92	5.04e-02	1.00	1.88e-03	1.92	3.02e-01	1.00
	128	8.75e-05	1.96	2.52e-02	1.00	4.82e-04	1.97	1.51e-01	1.00
	256	2.21e-05	1.98	1.26e-02	1.00	1.22e-04	1.98	7.56e-02	1.00
SIPGD-L, 2	32	2.19e-05	—	5.10e-03	—	1.32e-04	—	3.06e-02	—
	64	2.72e-06	3.01	1.28e-03	2.00	1.63e-05	3.01	7.66e-03	2.00
	128	3.40e-07	3.00	3.19e-04	2.00	2.04e-06	3.00	1.91e-03	2.00
	256	4.25e-08	3.00	7.98e-05	2.00	2.55e-07	3.00	4.79e-04	2.00
SWIPD-L, 1	32	1.29e-03	—	1.01e-01	—	7.14e-03	—	6.05e-01	—
	64	3.41e-04	1.92	5.04e-02	1.00	1.88e-03	1.92	3.02e-01	1.00
	128	8.75e-05	1.96	2.52e-02	1.00	4.82e-04	1.97	1.51e-01	1.00
	256	2.21e-05	1.98	1.26e-02	1.00	1.22e-04	1.98	7.56e-02	1.00
SWIPD-L, 2	32	2.19e-05	—	5.10e-03	—	1.32e-04	—	3.06e-02	—
	64	2.72e-06	3.01	1.28e-03	2.00	1.63e-05	3.01	7.66e-03	2.00
	128	3.40e-07	3.00	3.19e-04	2.00	2.04e-06	3.00	1.91e-03	2.00
	256	4.25e-08	3.00	7.98e-05	2.00	2.55e-07	3.00	4.79e-04	2.00

Table 2 Ex. 1 in 3D: EOC for L^2 and H^1 errors for $A = 0.1$ and $\tau = 10^{-3} \cdot 2^{-\frac{N-8}{8}}$.

Scheme	p	N	L^2		H^1	
			Error	EOC	Error	EOC
SIPGD-L	1	8	5.50e-03	—	3.48e-01	—
		16	1.40e-03	1.97	1.76e-01	0.98
		32	3.51e-04	1.99	8.76e-02	1.01
		64	8.80e-05	2.00	4.37e-02	1.00
SWIPD-L	1	8	5.50e-03	—	3.48e-01	—
		16	1.40e-03	1.97	1.76e-01	0.98
		32	3.51e-04	1.99	8.76e-02	1.01
		64	8.80e-05	2.00	4.37e-02	1.00

For the remainder of the numerical experiments, we employ the SWIPD-L scheme with $\alpha = \frac{1}{2}$, as it yields a more diffusive flux and consequently improved consistency. Furthermore, we use $\beta = 3$ for the mobility flux as in Rmk. 1.

Example 2 (Merging droplets) We consider the CH equations without advection, i.e., $\mathbf{u}(\cdot, \cdot) = \mathbf{0}$, in the domain $\Omega = [0, 1]^2$. The initial condition is given by a smooth profile

$$\psi(\mathbf{x}, 0) = (1 - 10^{-8}) \left(2 \max \left\{ \left(1 + 2^{-1} \sum_{j=1}^2 \tanh \left(\frac{r - \|\mathbf{x} - \mathbf{c}_j\|}{\sqrt{2}Cn} \right) \right), 1 \right\} - 1 \right), \quad (26)$$

where $r = 0.2$ is the droplet radius, with central points $\mathbf{c}_1 = (0.3, 0.5)^T$ and $\mathbf{c}_2 = (0.7, 0.5)^T$, Cahn number $Cn = 4h_{\min}$, and Peclet number $Pe^{-1} = 3Cn$. The simulation is run for $t \leq T = 0.4$.

Example 3 (Rotating Merging Bubbles) We consider the CHNS equations in the domain $\Omega = [-0.5, 0.5]^2$, with a divergence-free initial velocity field

$$\mathbf{u}(\mathbf{x}, 0) = \chi \left(x_2 \left(0.16 - \|\mathbf{x}\|^2 \right)_{\oplus}, -x_1 \left(0.16 - \|\mathbf{x}\|^2 \right)_{\oplus} \right), \quad (27)$$

where $\mathbf{x} = (x_1, x_2)^T$, and $\chi = 100$ is a scaling factor. The initial phase-field profile is

$$\psi(\mathbf{x}, 0) = 0.995 \left(0.5 \max \left\{ 4, 2 + \sum_{j=1}^2 \tanh \left(\frac{r_j - \|\mathbf{c}_j - \mathbf{x}\|}{\sqrt{2}Cn} \right) \right\} - 1 \right), \quad (28)$$

where $r_1 = 0.25$ and $r_2 = 0.15$ are the radii of the respective droplets, with central points $\mathbf{c}_1 = (0.1, 0.1)^T$ and $\mathbf{c}_2 = (-0.15, -0.15)^T$, respectively. The following non-dimensional numbers are considered: Reynolds number $Re = 1$, Cahn number $Cn = 4h_{\min}$, Weber number $We = Cn^{-1}$, viscosities $\mu_1 = \mu_2 = 1$, densities $\rho_1 = 100$ and $\rho_2 = 1$, and Peclet number $Pe^{-1} = 3Cn$. The simulation is run for $t \leq T = 0.2$.

For Exs. 2 and 3, we consider an hp -adaptive formulation with $h_{\min} = \frac{1}{256}$ and $h_{\max} = \frac{1}{128}$ using the SWIPD-L scheme and a prescribed maximum polynomial degree of p_{\max} and $p_{\min} \geq 0$. For the time increments, following [8], we set $\tau = 10^{-3}$ for Ex. 2 and $\tau = 5 \cdot 10^{-4}$ for Ex. 3. We simulate with different order levels of p for p -adaptivity and also compare to only the h -adaptive formulation, i.e., $p = p_{\max}$ for all elements $K \in \mathcal{T}_h$. We observe that convergence was not achieved for Ex. 2 with $p = 2$ for the h -adaptive formulation; convergence was only obtained, in that case, when $\|\psi_h\|_{L^\infty(K)} \lesssim 1$, as was also stressed in [8] regarding careful selection of the initial data. To the best of the authors' knowledge there is no clear proof or indication on how to find a safe initial value. Figure 3 shows the energy, mass, and boundedness for Ex. 2 using the hp -adaptive formulation of SWIPD-L with for various p -levels for hp -adaptivity. The energy is monotonically non-increasing, mass is conserved, and the phase-field remains bounded, consistent with the theoretical properties. The results are similar to those obtained using only h -adaptivity with $p = 1$, and for $p_{\max} = 1$ with hp -adaptivity, which suggests that the hp -adaptive formulation preserves

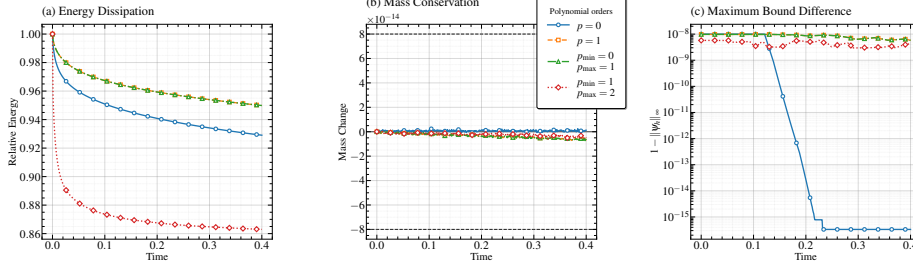


Fig. 3 Ex. 2: Energy, mass, and boundedness for SWIPD-L.

accuracy alongside the h -adaptive formulation, while providing a significant reduction in complexity and degrees of freedom. Figure 4 shows that the energy is non-increasing,

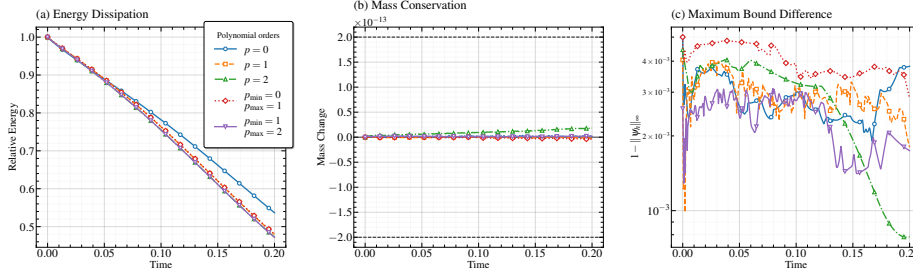


Fig. 4 Ex. 3: Energy, mass, and boundedness for SWIPD-L.

mass is conserved, and the phase-field remains bounded for Ex. 3 using the hp -adaptive formulation of SWIPD-L with and without p -adaptivity for the studied levels. The results are similar to those obtained using only h -adaptivity for the studied p -levels, which further indicates that the hp -adaptive formulation preserves physical accuracy alongside to the h -adaptive formulation, while providing a significant reduction in complexity and degrees of freedom, similarly to our discussion for Ex. 2. We also note that for $p = 2$ the mass difference in Fig. 4 is slowly increasing due to the nonlinear tolerance ϵ (for these simulations we picked $\epsilon = 5 \cdot 10^{-16}$) having to be picked slightly larger to avoid solver stagnation. These minor mass drifts are a known issue with potential deviations scaling as the non-linear tolerance as noted in [8]. Regardless, as is seen in Figs. 3 and 4 showing that the mass change is negligible in comparison to the lines at $\Delta m = \pm \frac{T}{\tau} \epsilon$ for $\epsilon = 2 \cdot 10^{-16}$ for Ex. 2 and $\epsilon = 5 \cdot 10^{-16}$ for Ex. 3.

4 Summary and Outlook

We have proposed a new class of DG schemes for the CH equations with degenerate mobility has been proposed, which are provably coercive and stable under a certain

condition on the mobility flux for the penalty term. The introduced mobility flux formulations for the penalty term include SIPGD-L, which employs the intersection maximum of the mobility, and SWIPD-L, which uses a harmonic average. These mobility fluxes yield similar estimates for the coercivity condition and accuracy as previous schemes. Numerical experiments illustrate the performance of the proposed schemes, demonstrating that they achieve optimal convergence rates and that the harmonic mobility flux provides potentially significant improvements in stability and accuracy compared to the arithmetic mean. An hp -adaptive formulation has also been presented, showing significant reductions in complexity and degrees of freedom compared to the h -adaptive formulation while maintaining similar accuracy and physical fidelity.

Future work includes extending the theoretical analysis to provide rigorous proofs of boundedness for the SWIPD-L scheme in the broken Sobolev (DG) setting, exploiting the connection between the harmonic average and the minimum to extend Theorem 1. Additionally, more challenging test cases, such as the rising bubble benchmark, will further validate the performance of the proposed schemes for coupled CHNS systems and assess adaptivity effects under more demanding conditions.

References

1. Ainsworth, M., Rankin, R.: Constant free error bounds for nonuniform order discontinuous Galerkin finite-element approximation on locally refined meshes with hanging nodes. *IMA Journal of Numerical Analysis* **31**(1), 254–280 (2009). DOI 10.1093/imanum/drp025
2. Bastian, P., Blatt, M., Dedner, M., Dreier, N.A., Engwer Ch. Fritze, R., Gräser, C., Grüninger, C., Kempf, D., Klöfkor, R., Ohlberger, M., Sander, O.: The Dune framework: Basic concepts and recent developments. *CAMWA* **81**, 75–112 (2021). DOI 10.1016/j.camwa.2020.06.007
3. Dedner, A., Klöfkor, R.: Extendible and Efficient Python Framework for Solving Evolution Equations with Stabilized Discontinuous Galerkin Method. *Commun. Appl. Math. Comput.* (2021). DOI 10.1007/s42967-021-00134-5
4. Dedner, A., Klöfkor, R., Nolte, M.: Python bindings for the dune-fem module (2020). DOI 10.5281/zenodo.3706994
5. Elliott, C.M., Garcke, H.: On the Cahn–Hilliard equation with degenerate mobility. *Siam Journal on Mathematical Analysis* **27**(2), 404–423 (1996). DOI 10.1137/S0036141094267662
6. Epshteyn, Y., Rivière, B.: Estimation of penalty parameters for symmetric interior penalty Galerkin methods. *Journal of Computational and Applied Mathematics* **206**(2), 843–872 (2007). DOI 10.1016/j.cam.2006.08.029
7. Ern, A., Stephansen, A.F., Zunino, P.: A discontinuous galerkin method with weighted averages for advection–diffusion equations with locally small and anisotropic diffusivity. *IMA Journal of Numerical Analysis* **29**(2) (2008). DOI 10.1093/imanum/drm050
8. Gunnarsson, J.K., Klöfkor, R.: Comparison of Structure Preserving Schemes for the Cahn–Hilliard–Navier–Stokes Equations with Degenerate Mobility and Adaptive Mesh Refinement (2026). DOI arXiv:2602.08639v2. URL <https://arxiv.org/abs/2602.08639>
9. Rivière, B.: Discontinuous Galerkin methods for solving elliptic and parabolic equations: theory and implementation. *SIAM* (2008). DOI 10.1137/1.9780898717440
10. Zhang, X., Shu, C.W.: On maximum-principle-satisfying high order schemes for scalar conservation laws. *Journal of Computational Physics* **229**(9), 3091–3120 (2010). DOI 10.1016/j.jcp.2009.12.030